UAV Remotely-Powered Underground IoT for Soil Monitoring

Yu Luo, *Member, IEEE* and Lina Pu, *Member, IEEE*

***Abstract*— This article introduces a practical approach to wirelessly charge underground Internet of things (UIoT) for soil monitoring using ultra high frequency (UHF) radio energy. In the proposed system, UIoT nodes do not require batteries or any aboveground attachments (e.g., solar panel). Instead, they harvest 915 MHz radio energy emitted from an unmanned aerial vehicle (UAV) for semi-perpetual operation. The UIoT nodes utilize the harvested energy to measure soil parameters and transmit data back to the UAV using ZigBee protocol. After collecting the data from UIoTs, the UAV uploads it to a cloud server for online soil quality analysis. The system has been optimized for efficient operation, with a UAV transmit power as low as 2 watts. Startup, drive, and power management circuits have been designed to ensure reliable operation of UIoT nodes, even with low incident energy. According to experimental results, the developed RF-UIoT system can successfully power up and transmit more than 1 kilobyte of data within 10 seconds of wireless charging, followed by an additional 1.7 kilobytes of data every 1.6 seconds thereafter.**

***Index Terms*—Radio energy charging, underground Internet of things (UIoT), soil monitoring for industrial agriculture.**

I. INTRODUCTION

Soil is the foundation of agriculture and forestry, both of which are essential for humanity. The health of the soil is critical as it directly impacts food production and terrestrial ecosystems. Unfortunately, soil health is vulnerable to degradation due to agricultural and industrial activities, such as poor farm management and pollutant emissions [1].

To promote the sustainability and productivity of industrial agriculture, long-term monitoring of soil conditions, including moisture, pH value, and nutrition, is crucial. Traditional approaches to collecting soil samples for laboratory measurement are time-consuming and labor-intensive [2]. The application of remote sensing techniques for soil moisture mapping has experienced substantial growth in recent years [3]. Nevertheless, many soil properties, such as pH, conductivity, and organic matter, cannot be accurately assessed through non-contact measurements [4].

Underground Internet of things (UIoT) is emerging as a promising technique for long-term, scalable, and automated *in situ* soil monitoring. However, current soil sensors predominantly depend on solar energy or battery power [5], [6]. Solar-powered sensors necessitate aboveground deployment, interfering with tillage or crop harvesting, while battery-powered sensors demand frequent battery replacements. Identifying sustainable and scalable power sources for underground IoT devices remains a significant challenge hindering the adoption of soil sensors. To facilitate large-scale soil monitoring networks, battery-free and aboveground attachment-free soil sensors are desired.

The above goal can be realized by developing Radio Frequency charging-enabled underground IoT (RF-UIoT). We envision a system that leverages Unmanned Aerial Vehicles (UAVs) to remotely power UIoT devices. As illustrated in Fig. 1, the RF-UIoT nodes do not have batteries or any aboveground attachments, such as solar panels. The UAV, equipped with an ultra high frequency (UHF) RF transmitter, navigates the field and remotely charges the RF-UIoTs. The underground nodes utilize the harvested RF energy to sense the environment and transmit sensing results to the UAV. Upon gathering data from RF-UIoTs, the UAV forwards it to a cloud server via the internet for real-time soil quality analysis. Compared to unmanned ground vehicle (UGV), UAVs offer faster and more versatile operation, unrestricted by topographical features, enabling large-scale soil monitoring. Consequently, UAVs are chosen to serve as both mobile energy sources and data mules for RF-UIoTs.

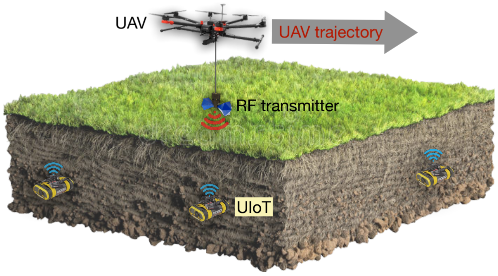

Figure 1: UAV remotely charging RF-UIoTs that do not have batteries or any aboveground attachments (i.e., solar panel).

In recent decades, harvesting weak radio energy in the UHF band has been widely explored in both industry and academia [7], [8]. However, current applications of RF energy harvesting primarily focus on airborne scenarios, where harvesters capture ambient RF energy emitted from TV towers or cellular base stations to power ultra-low-power wireless devices [9], [10]. The concept of utilizing UHF radio wave to charge underground IoT devices is introduced in [11] and [12]. A proof-of-concept demonstration is presented in [13], employing the Powercast P2110-EVAL-01 energy harvester.

A. Limitations of Today's Approach

According to our experiment results, the existing RF energy harvesters [11]–[13] can not be directly applied to practical underground IoT applications due to the following challenges:

1) Dropping supply voltage: Due to the limited energy storage capacity of RF-UIoT nodes (e.g., 1 mF capacitor)

This work was supported in part by the US National Science Foundation under Awards CIF-2051356, CNS-2122167, and CNS-2122159.

Yu Luo is with Department of Electrical and Computer Engineering, Mississippi State University. Email: yu.luo@ece.msstate.edu. Lina Pu is with Department of Computer Science, University of Alabama. Email: lina.pu@ua.edu.

resulted from low RF harvesting rates, the voltage of the energy storage, which also serves as the RF-UIoT's supply voltage, may experience a significant drop during startup, sensing, and transmission processes. In contrast to the constant voltage and current during startup observed in lithium battery-powered UIoT, RF-UIoT nodes exhibit substantial supply voltage and system current reduction, as shown in Fig. 2. Without a specialized charging control circuit, current RF-UIoT cannot reliably start up[1]. To address this issue, we will design a startup circuit compatible with existing RF energy harvesters.

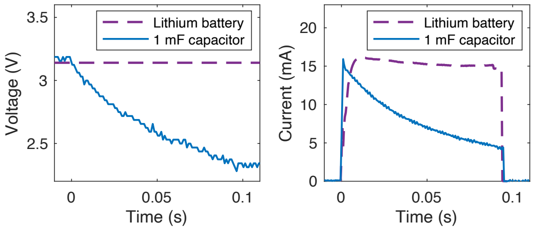

Figure 2: Dropping supply voltage during Startup process.

2) High signal attenuation in soil: The propagation attenuation of radio waves is considerably higher in the soil compared to air. Consequently, the transmit power of the UAV should be sufficiently high to ensure that radio waves can reach sensor nodes embedded in the soil. However, limitations in the UAV's energy supply and payload necessitate an efficient energy emission strategy for improved charging efficacy. To overcome this challenge, we will propose a pulse charging strategy for RF-UIoT in Section II.

3) Dynamic energy consumption: Apart from the startup process, other energy-intensive operations, such as communication, can also lead to a substantial supply voltage drop, resulting in dynamic energy consumption. This issue is unique to RF-UIoT and is not present in battery-powered devices. Motivated by this distinct phenomenon, we will analyze the power consumption of RF-UIoT during startup, transmission, and sensing processes in Section III.

B. Contributions of This Work

We built a RF-UIoT prototype using off-the-shelf RF energy harvester and wireless board, and custom-designed startup, drive and power management circuits. Experimental results demonstrate that the RF transmitter's power consumption can be as low as 2 W to wirelessly charge sensor nodes at a minimum depth of 15 cm underground in the 915 MHz frequency band. Each RF-UIoT employs a 1 mF aluminum electrolytic capacitor for energy storage. The UAV is capable of powering up the RF-UIoT with 10 seconds of wireless charging. Upon activation, the node can perform at least 100 soil property measurements and subsequently transmit over 1 KB of sensed data to the UAV at a rate of 1 Mbps using the ZigBee protocol. In scenarios requiring continuous data transmission, the RF-UIoT can transmit an additional 1.7 KB of data following 1.6 seconds of energy harvesting, or 2.9 KB of data every 3 seconds.

The major contributions of this article lie in the following aspects:

a) We develop startup & drive circuits to enable RF-UIoT reliably startups at low incident energy. Our proposed startup and drive circuits achieve an 8.1 dBm improvement (-2 dBm with the circuits compared to 6.1 dBm without them).

b) We propose a pulse charging strategy enhance the charge efficiency. Pulse charging experiments are conducted with varying incident power, pulse width, and duty cycles. According to experiment results, the charging time can be reduced from 15 s to 10 s when utilizing a 5% duty cycle.

c) We analyze the dynamic power consumption of RF-UIoT and design a power management module to improve energy efficiency. With the power management circuit in place, RF-UIoT can dynamically adjust data transmission and sleep timings according to the residual energy of battery and communication workload.

d) A system integration test is performed using the custom-designed startup, drive, and power management circuits, Powercast TX91503 energy source, Powercast P1110B harvester, and Microchip ATmega256RFR2 wireless board. All proposed solutions (e.g., startup, drive, and power management) except pulse charging are verified in the system integration test. Furthermore, we evaluate pulse charging, startup, drive, and power management components separately in controllable lab experiments in order to evaluate their performance.

The rest of the article is organized as follows. In Section II, we conduct experiments to measure the strength of radio energy in the soil. The power consumption of sensor nodes is analyzed in Section III. In Section IV, we introduce the circuit design to make RF-UIoT operate reliable in real applications. We introduce the related work in Section V and conclude this article in Section VI.

II. REMOTELY-POWERING UIOT USING UAV

This section validates the feasibility of charging underground sensor nodes via UHF radio waves. We begin by measuring the strength of radio energy in soil. Subsequently, a pulse charging strategy is proposed to efficiently power nodes in deeper deployments (greater than 30 cm) without negatively impacting the UAV's battery life.

A. Feasibility of using UAV to Wirelessly Charge UIoT

In this article, we choose 915 MHz radio energy to charge RF-UIoT. Compared with the 433 MHz frequency band commonly used for underground wireless communication [14], [15], the propagation attenuation of radio waves with higher frequencies in the soil is larger, but the size of the receiving antenna can be significantly reduced, which is attractive for large-scale deployment.

---

[1] Our experimental results indicate that incident power must exceed 6.1 dBm to power the wireless board using the Powercast P1110B energy harvester, rendering it impractical for real underground applications.

To understand the strength of RF energy in the soil, we used a Powercast TX91503 transmitter carried by a DJI Matrice 600 Pro drone to emit 915 MHz continuous wave through a patch antenna. The power consumption of the RF transmitter was 2 W and the antenna gain was 8 dBi. The effective isotropic radiated power (EIRP) of the transmitter was 36 dBm (3 W). The drone used a real-time kinematic positioning (RTK) system for accurate localization and attitude adjustment. In the experiment, the volumetric water content (VWC) and the electrical conductivity (EC) were measured using the BlueLab soil meter; other *in-situ* soil sample properties was tested in the laboratory. The key parameters of the soil[2] are listed in Table I.

Table I: *In-situ* soil sample properties

Sample depth	Texture	VWC	EC	Clay	Silt	Sand
15 cm	Silt loam	40%	80 mS/m	11%	53%	36%

The experimental scene is demonstrated in Fig. 3(a), where a remotely controllable mini winch connected the drone and the TX91503 transmitter to flexibly adjust the distance between the transmitter and the ground. In the experiment, the flight attitude of drone was 1.6 m and the TX91503 transmitter was hung approximately 4 cm above the ground to achieve the best charging performance. The average wind speed during the experiment was 11 mph.

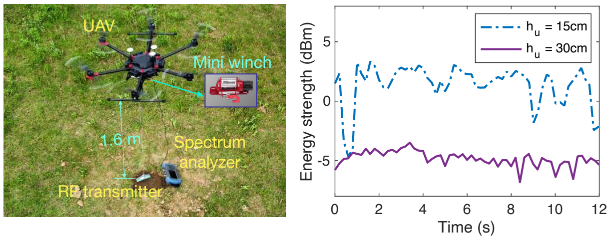

(a) (b)

Figure 3: Radio energy in the soil. (a) Experimental setup. (b) Intensities of received energy, where h_u is the buried depth.

In Fig. 3(b), we show the strength of RF energy received by sensor nodes buried in different depths of the soil, where an omnidirectional patch antenna with 0 dBi gain was used to receive energy. From the figure, it can be observed that the average intensity of the received energy can reach 2 dBm and -5 dBm for nodes buried 15 cm and 30 cm underground, respectively. In addition, due to the disturbance of wind, the attitude of the drone and the hanging height of the transmit antenna fluctuate. As a result, the received energy strength was not constant but varied over time.

According to the literature review, the sensitivities of most RF energy harvesters are higher than -10 dBm [7]. Therefore, it is feasible to wirelessly charge nodes buried 15 cm or even deeper in the soil through UAVs.

B. Pulse Charging Strategy

The energy harvesting rate of RF-UIoT is determined by the intensity of incident energy. To reduce the charging time, the UAV can increase the transmit power, which requires more energy supply and a larger heat sink. However, the UAV's battery life and payload are limited. To not compromise the coverage of the UAV for large-scale data collection, we can use modulated pulse train to improve the charge efficiency. Specifically, instead of emitting a continuous wave, the transmitter broadcasts pulse train modulated by 915 MHz carrier signal.

In the experiment, we simply use a square wave as the envelope of the pulse energy. This is because the pulse width used in the experiment ($>$ 10 ms) is much longer than the carrier signal period (1.1 ns at 915 MHz). If the pulse width is short, a sinc function should be used as the envelope to prevent energy leakage from sidelobes of the modulated pulse in the spectrum.

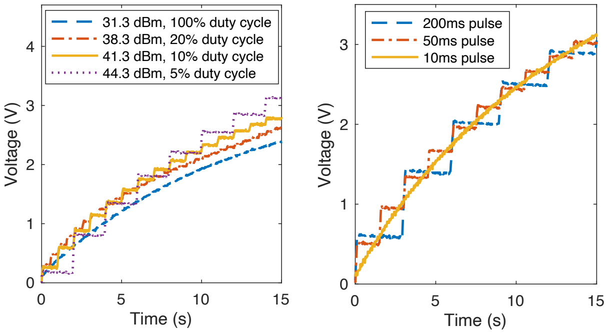

(a) (b)

Figure 4: Pulse Charing with 1 mF capacitor. (a) Different duty cycles and EIPRs. (b) Different pulse widths.

In Fig. 4, we study the impact of the pulse pattern on the charging rate. In the experiment, we used a Powercast P1110B harvester[3] to receive RF energy [19]. When the incident power is between -2 dBm and 10 dBm, the energy conversion efficiency of the harvester varies from 55% and 65%. The node is buried 15 cm in the soil and store the received energy in a 1 mF aluminum electrolytic capacitor. Several different pulse trains are constructed by varying the incident power, pulse width, and duty cycle. The total energy consumed by the UAV broadcasting different pulse trains is exactly the same because we will increase the transmit power and decrease the duty cycle of the pulse train at the same time.

In Fig. 4(a), the pulse width is fixed at 100 ms. As can be observed from the figure, the use of a high power but low duty cycle pulse train can significantly increases the charging rate. For example, when the EIPR of the RF transmitter is 31.3 dBm (1.35 W) and the duty cycle of the pulse train is 100% (continuous wave), the strength of the energy received by UIoT nodes is around -1.5 dBm (i.e., 0.708 mW). In this

---

[2] The impact of soil type and soil moisture on the propagation of RF energy in soil can refer to the Aboveground-to-underground (AG2UG) channel models in the literature [16], [17].

[3] Compared to Powercast P2110B, P1110B has lower sensitivity but higher energy efficiency [18], [19]. In our application scenario, the input power is expected to be between 0 dBm and 15 dBm with pulse charging. The sensitivity of energy harvester is not a concern. Therefore, we choose to use P1110B harvester for higher energy conversion efficiency.

case, it takes the transmitter 15 s to charge the capacitor to 2.4 V. However, the charging time is reduced by 5 s when the transmitter's EIPR is increased to 44.3 dBm (26.9 W) and the duty cycle is decreased to 5%. Next, we briefly analyze this observation.

According to [20], an RF energy harvester with an energy storage capacitor can be modeled as an RC circuit connected to a direct current (DC) power supply. As the incident power increases, the resistor's resistance decreases, while the output voltage of the DC power supply raises. In this case, the time constant of the RC circuit (the product of resistance and capacitance) is inversely proportional to the received energy intensity. Therefore, using a high-power, low-duty-cycle pulse train can charge the RF-UIoT faster than a low-power, high-duty-cycle one, despite the same energy consumption for transmitting both trains.

In Fig. 4(b), we fix the EIPR of the RF transmitter and the duty cycle of the pulse train to 43 dB (20 W) and 6.7%, respectively, and then evaluate the effect of pulse width on the RF-UIoT charging rate. As shown in the figure, the pulse width does not affect the charging rate. However, transmitting short pulses can greatly reduce heat dissipation requirements, thereby reducing the size and weight of the transmitter to increase the battery life of the UAV.

Note that when the same charging pattern (e.g., energy intensity, duty cycle, etc.) is used, the time to charge the capacitor to a given voltage is linearly proportional to the capacity of capacitor. We used 1 mF capacitor for demonstration purpose. Similar conclusion can be drawn to capacitors of different capacities.

III. Power Consumption Analysis for RF-UIoT

In this section, we analyze the power consumption of underground sensor nodes in different modes. The results obtained in this section will be used to design a dedicated control circuit to maximize the energy harvesting efficiency and energy utilization of RF-UIoT nodes.

In this article, we choose the Microchip ATmega256RFR2 microcontroller (MCU) as the backbone of our underground node [21]. The selected MCU has an integrated 2.4 G wireless module that supports IEEE 802.15.4 Zigbee protocol. In the deep sleep mode, the quiescent current of the MCU is only 650 nA. Therefore, we just focus on the energy consumption on startup, data sampling, and wireless transmission.

A. Startup Energy Consumption

Startup is one of the most energy consuming processes in RF-UIoT that will cause significant voltage drop. Fig. 5 evaluates the effect of supply voltage and clock frequency on current and energy consumed by MCU startup. In Fig. 5(a), the MCU clock frequency was fixed at 1 MHz. As shown in the figure, as the supply voltage grew, the startup current greatly increased. Specifically, when the supply voltage was 2.76 V, the average startup current was only 5.4 mA. However, when the supply voltage increased to 3.25 V, the current increased by 307% to 22 mA.

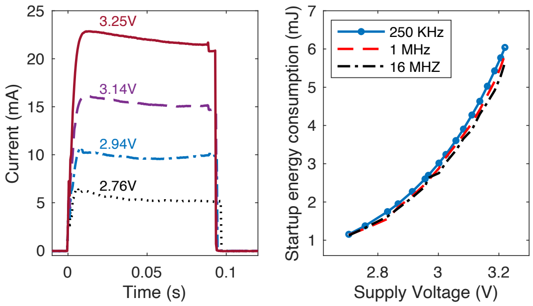

Figure 5: Energy consumed to start the IoT node. (a) Current waveforms at 1 MHz clock rate. (b) Energy consumptions in different conditions.

In Fig. 5(b), we examine the impact of the clock rate and the supply voltage of the MCU on the energy consumption during startup, which is the integral of startup current multiplied by the supply voltage over time. As can be observed from the figure, when the supply voltage was 2.7 V, the MCU consumed only 1.1 mJ to power up. However, once the voltage increased to 3.2 V, the energy consumption rapidly increased to 6 mJ, which was five times higher than the previous case. Also, using a high clock frequency to drive the MCU can slightly reduce energy consumption at startup, especially when the supply voltage is high. For instance, when the supply voltage is 3.2 V, if we increase the clock frequency of the MCU from 250 kHz to 16 MHz, the energy consumption can decrease from 6 mJ to 5.6 mJ.

B. Transmission Energy Consumption

The energy consumption on data transmission is sensitive to both MCU clock frequency and transmission power. In Fig. 6, we present the current waveforms as the MCU sends data at different settings. In the experiment, the MAC service data unit (MSDU) payload was 105 octets, the supply voltage was 2 V, and the data rate was fixed at 250 kbps. As shown in the figure, the waveform can be divided into two stages: (a) Transmission preparation, and (b) data transmission. Let T_p and T_t be the durations of the preparation stage and the transmission stage, respectively. T_p contains the time to push the transceiver into transmit mode, which includes ramping up the voltage regulator and initializing the phase-locked loop (PLL). T_t consists of the time to send the protocol headers and MSDU payload.

From Fig. 6, we have three major observations. First, the clock rate and the transmit power does not affect the current consumption in the first stage. However, the preparation time is proportional to the MCU clock frequency. Specifically, when the clock rate is reduced from 1 MHz to 250 kHz, the preparation time increases from 2.8 ms to 9.6 ms.

Second, the clock frequency does not affect the transmission time. However, at a given transmit power, the current consumption in the second stage is not constant but is affected by the clock frequency. Specifically, when the clock frequency is 250 kHz and the transmit power is 3.5 dBm, the average current during data transmission is only 15.1 mA. However, at

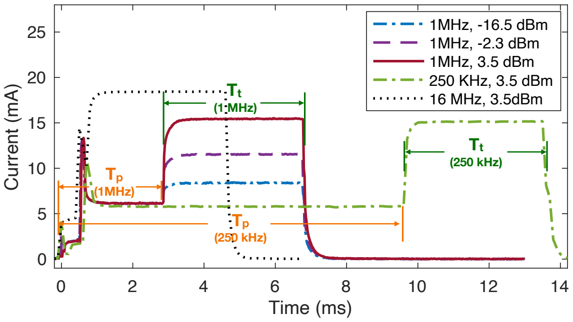

Figure 6: Current waveforms of the underground node during data transmission.

the same transmit power, if the clock rate is set to 16 MHz, the current consumption increases to 18.4 mA.

Third, at a given clock rate, the current consumption in the second stage increases nonlinearly with the increase of the transmit power. Specifically, when the clock rate is fixed at 1 MHz, the current consumption is 8.4 mA to send data at -16.5 dBm (22 μW). If we increase the transmit power one hundred time to 3.5 dBm (2.2 mW), the current consumption only increases by 1.8 times to 15.1 mA.

Table II: E_t change with f_c.

f_c (MHz)	0.125	0.25	0.5	1	2	4	8	16
E_t (μJ)†	330	228	178	154	150	144	150	154

† In this experiment, the supply voltage is 2 V, the MSDU payload is 105 octets, the transmit power is 3.5 dBm, and the data rate is 250 kbps.

According to the above observations, when the clock frequency is low, more energy is required to prepare for transmission but less energy is required for sending data. Therefore, given the transmit power and data rate, there is an optimal clock frequency that minimizes the energy consumption in data transmission. To verify this, let f_c and E_t denote the clock frequency and energy consumption of sending a data packet, respectively. We measure E_t at different f_c. As listed in Table II, E_t does not decrease monotonically with f_c, but reaches a minimum value at a clock frequency of 4 MHz.

In addition to the clock frequency, the supply voltage also affects the energy consumption of sending data. According to experimental results, the current consumption during preparation and data transmission is affected by the supply voltage. However, energy is the integral of current multiplied by voltage over time. As a result, the energy consumption increases linearly with supply voltage.

C. Sampling Energy Consumption

In Fig. 7, we measure the energy consumption of the MCU to sample the data through a 10-bit analogue to digital converter (ADC). The ADC clock frequency is half the MCU clock frequency. It can be observed from Fig. 7(a) that the current of ADC sampling includes two phases: (a) ADC warmup with duration T_w. (b) Data convention with duration T_s. As shown in the figure, increasing the MCU clock frequency only slightly reduces T_w, but can significantly shorten T_s, thereby reducing the energy consumption of data sampling. The reasons are analyzed below.

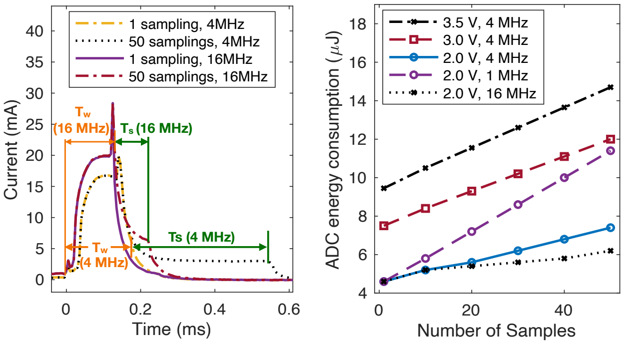

Figure 7: ADC energy consumption. (a) Current waveforms of ADC with different clock frequencies and number of samples. (b) Energy consumption of ADC with different clock frequencies and supply voltage.

The first phase contains the time to power up the analog voltage regulator and that to start ADC. The former is a constant, which is about 110 μs measured in our experiments; the latter defaults to 84 ADC clock cycles, which are 42 μs and 10.5 μs at 4 MHz and 16 MHz MCU clock frequencies, respectively. Therefore, using a high clock frequency to drive the MCU does not reduce T_w much.

The second phase includes the ADC startup delay, data conversion time, and tracking time, which are 2 CPU clock cycles, 11 ADC clock cycles, and 2 ADC clock cycles, respectively. Accordingly, the length of T_s is 14 clock cycles multiplied by the number of samples. Given the number of samples, T_s increases linearly with the MCU clock frequency. As shown in Fig. 7(a), if the ADC samples 40 times, T_s are about 350 μs and 87.5 μs at 4 MHz and 16 MHz MCU clock frequencies, respectively.

In addition to the clock frequency, the supply voltage also affects the energy consumption of the ADC. As depicted in Fig. 7(b), if the MCU clock frequency is 4 MHz and the supply voltage is 2 V, the ADC spends 7.4 μJ of energy for 40 samples. For the same clock frequency and number of samples, if the supply voltage is increased to 3.5 V, the energy consumption increases to 14.7 μJ, almost doubling.

D. Summary

The startup process generally consumes much more energy than transmitting data or sensing. Take the low-power Microchip ATmega256RFR2 node as an example, the startup at 2.7 V, transmitting 105 octets data, and sampling 40 times consume 1.1 mJ, 144 μJ, and 7.4 μJ, respectively. The high startup energy consumption will significantly drive down the supply voltage of RF-UIoT, causing startup failure when the ATmega256RFR2 board is directly connected to the RF energy harvester. Therefore, a dedicated control circuit is required to reliably activate the underground UIoT node with the thin RF energy, which will be introduced in the next section.

IV. CIRCUIT DESIGN FOR RF-UIOT

In this section, we design a dedicated control circuit for RF-UIoT based on the observations discussed in previous sections.

It allows the node to efficiently utilize the energy harvested from the UAV for reliable startup, sensing and communication.

A. Startup Circuit

Before introducing the details of the control circuit, we need to first clarify that the MCU cannot be directly connected to the energy storage capacitor; otherwise, it will automatically enter the startup procedure when the capacitor's voltage rises to a threshold, which is 1.8 V for ATmega256RFR2. However, as described in Section II-A, the average energy harvesting rate of RF-UIoT is less than 1.6 mW (2 dBm), which is much lower than the power consumption (9 mW at 1.8 V supply voltage) required for startup. As a result, the MCU will continuously consume the received energy but never be successfully activated.

To solve the above problem, we use a Schmitt trigger as the startup circuit, which turns on at V_{on} and turns off at V_{off}. With a high V_{on}, the startup process of the MCU can be properly delayed, allowing the capacitor to accumulate enough energy to activate the system. With a low V_{off}, the MCU can fully utilize the energy stored in the capacitor until the voltage drops to 1.8 V.

As shown in Fig. 8, let V_{cc} be the supply voltage provided by the energy storage capacitor $\mathrm{C_s}$. Unlike battery-powered devices, the V_{cc} of RF-UIoT varies quickly with the energy harvesting process and node activities. Therefore, the fixed reference voltage required by conventional Schmitt triggers is unavailable in our application. To this end, we use the capacitor $\mathrm{C_1}$ and diode $\mathrm{D_1}$ to create a dynamic reference voltage at the inverting input of the comparator $\mathrm{CP_1}$. At the non-inverting input, resistors $\mathrm{R_1}$ and $\mathrm{R_x}$ form a voltage divider network to generate a comparison signal.

When V_{cc} is small, V_+ is lower than V_-, and the output voltage of $\mathrm{CP_1}$ is 0. As V_{cc} rises, V_+ increases linearly with V_{cc}. At the same time, V_- also increases but slower than V_+ because of the nonlinear relationship between the forward voltage and the forward current of the diode. When V_{cc} reaches 3 V, the output of $\mathrm{CP_1}$ is toggled since V_+ catches up with V_-. In this case, the feedback resistor $\mathrm{R_2}$ is connected with $\mathrm{R_1}$ in parallel, and $\mathrm{R_x}$ obtains more voltages from the divider network. Consequently, when V_{cc} drops to 3 V, the Schmitt trigger can retain its output until the supply voltage is further reduced to 0.9 V, in which the $\mathrm{D_1}$'s forward voltage catches up with V_+.

Regarding the startup circuit, we emphasize two points. First of all, the capacitor $\mathrm{C_1}$ cannot be replaced by a resistor used in a regular diode-based reference. This is because the startup circuit is connected to the driver, which will dissipate a large amount of energy at the instant Schmitt trigger is turned on. As a result, if $\mathrm{C_1}$ is replaced by a resistor, V_{cc} will drop sharply, which has a probability of accidentally turning off the startup circuit. In contrast, $\mathrm{C_1}$ can serve as a voltage regulator, which can temporarily stabilize V_+ and V_- for a short time to improve the reliability of the circuit.

Second, the forward voltage of the diode decreases linearly with increasing temperature, making it easy to compensate for the temperature via a negative temperature coefficient (NTC) thermistor $\mathrm{R_x}$. According to the experimental results, $\mathrm{R_x}$ should be $10\,\mathrm{k}\Omega$ when the ambient temperature is 25°C, and needs to be decreased by $1\,\mathrm{k}\Omega$ for every 5°C increment in temperature.

With the help of the startup circuit, the Powercast P1110B harvester is able to reliably power up ATmega256RFR2 wireless board at low incident energy (i.e., -2 dBm). By contrast, when the harvester is directly connected to ATmega256RFR2 without a startup circuit, a high energy density (i.e., 6.1 dBm) is required to reliably start the MCU.

B. Drive Circuit

The comparator may not generate enough sinking/sourcing current to directly drive a non-capacitive load, especially if the supply voltage is low and the load current is high. Moreover, the current consumption of the MCU in different modes varies greatly. Hence, a driver is needed to regulate the current according to the state of the MCU.

As shown in Fig. 8, the NPN transistor $\mathrm{T_2}$ is used to build the driver. Denote the voltage between the collector and emitter of $\mathrm{T_2}$ as V_{ce}. Let V_m be the supply voltage of the MCU, where $V_m = V_{cc} - V_{ce}$ and V_m must be greater than 1.8 V for reliable operation. In order to improve energy utilization, V_{ce} should be low to reduce the voltage loss of the transistor, so that the minimum V_{cc} can approach 1.8 V. To achieve this goal, we choose the transistor NSS30071, whose V_{ce} is less than 0.1 V at 1 mA base current and 100 mA collector current [22].

To drive RF-UIoT efficiently, the most challenging part is how to handle the high dynamic range of the MCU's current while minimizing system power consumption. Specifically, in deep sleep mode, the MCU's current consumption is only 650 nA. Therefore, pushing a small current at the base of $\mathrm{T_2}$ is sufficient to drive the MCU. In this situation, a large resistor can be added between the startup circuit and $\mathrm{T_2}$ to limit the current flowing through the base and emitter of $\mathrm{T_2}$, thereby reducing power consumption in sleep mode. In contrast, when the MCU starts up or sends data, as described in Section III, the current consumption could be over 20 mA, which is four orders of magnitude higher than the previous case. As a result, the base current at $\mathrm{T_2}$ must be increased so that more current can flow through the collector to appropriately drive the MCU. Thus, it is necessary to reduce the resistance of the resistor between the startup circuit and $\mathrm{T_2}$.

The above analysis indicates that the resistance between the startup circuit and $\mathrm{T_2}$ needs to be dynamically adjusted according to the states of the MCU. When the MCU is in deep sleep, the resistance should be large to reduce the power consumption of the driver. When the MCU starts up or transmits data, the resistance should be small to provide enough drive current for the MCU.

To achieve the above goal, two resistors, $\mathrm{R_3}$ and $\mathrm{R_5}$, are added between the output of $\mathrm{CP_1}$ and $\mathrm{T_2}$. As shown in Fig. 8, the resistance of $\mathrm{R_3}$ $(220\,\mathrm{k}\Omega)$ is much larger than $\mathrm{R_5}$ $(1\,\mathrm{k}\Omega)$. Next, we introduce how to short R_3 at the right time to adjust the drive current of the MCU for reliable startup and data transmission.

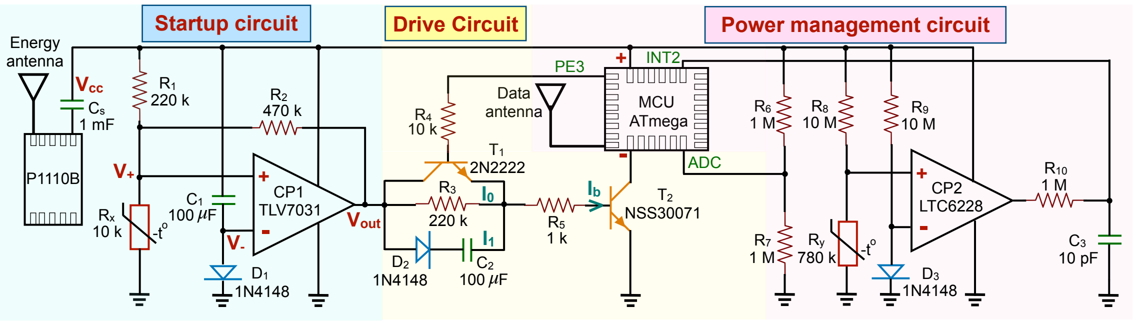

Figure 8: Control circuit of RF-UIoT.

1) Startup Driver: To provide MCU sufficient drive current for a successful startup, a diode D$_2$ and a capacitor C$_2$ are connected with R$_3$ in parallel. At the instant the startup circuit is turned on, the output of CP$_1$ (V_{out} in Fig. 8) immediately rises from 0 to V_{cc}. At this time, the resistance of C$_2$ is low and D$_2$ is turned on, thus shorting R$_3$. In this case, only R$_5$ is connected into the circuit. Therefore, T$_2$ can obtain a large current at the base to start the MCU. When C$_2$ is fully changed, D$_2$ is turned off and R$_3$ is automatically connected back to the circuit. As a result, the base current of T$_2$ decreases to save this energy.

The capacitance of C$_2$ must be moderate. If the capacitance is too large, the base current will remain high for a long time after the MCU is started, resulting in unnecessary energy consumption. However, if the capacitance is too small, the base current will drop for a short time, which may not be long enough for the MCU to complete the startup process. In order to successfully boot the system without wasting energy, the duration of high current at the base of T$_2$ should be approximately equal to the start time of the MCU, which is 95 ms described in Section III-A.

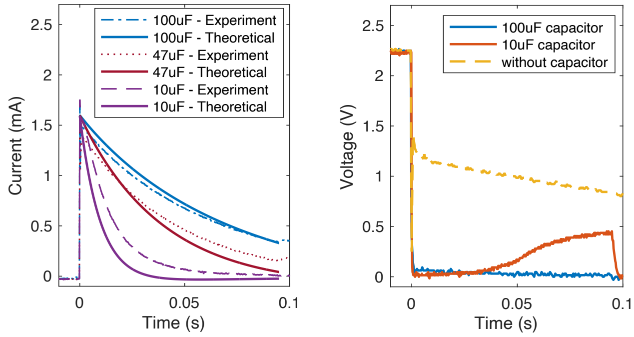

(a) (b)

Figure 9: Performance improvement with capacitor C$_2$ during MCU startup. (a) I_b of T$_2$. (b) V_{ce} of T$_2$.

In Fig. 9, we show how C$_2$ affects the performance of the startup driver. In the figure, the startup circuit is turned on when V_{cc} rises to 3 V at time 0. Let I_b be the base current at the collector of T$_2$. From Fig. 9 (a), it can be observed that using a large C$_2$ can significantly extend the duration of high I_b, which allows the T$_2$ to work in the saturation region for a while. In this case, there is only a small voltage drop between the emitter and collector of the transistor when the MCU starts up. By contrast, if C$_2$ is small, I_b will reduce quickly. Consequently, T$_2$ gradually enters the unsaturated region, resulting in a small drive current and large V_{ce} when the MCU starts up.

As depicted in Fig. 9(b), if C$_2$ is 100 μF, V_{ce} can be maintained at a small value (less than 30 mV) throughout the MCU startup process (from time 0 to 95 ms). However, if we reduce C$_2$ to 10 μF, V_{ce} can be small at first, but gradually increases as I_b in Fig. 9(a) drops below 0.2 mA. Finally, if C$_2$ is removed, V_{ce} will be high, causing insufficient drive current to successfully boot the MCU.

We can use a first-order non-homogeneous differential equation to describe I_b as a function of time and C$_2$. Let I_s represent the MCU startup current, which is not a constant by affected by the supply voltage. According to Fig. 5, the relationship between I_s and V_{cc} can be approximated by an exponential function:

$$I_s = \alpha e^{\beta V_{cc}}, \tag{1}$$

where $\alpha = 5.8 \times 10^{-6}$ and $\beta = 2.5$. In (1), V_{cc} is not constant but drops rapidly over time as the MCU consumes the energy stored in C$_s$ for startup.

According to (1) and the capacitor energy formula, it can be obtained the following equation set

$$\begin{cases} E(t) = \dfrac{1}{2} C_s V_{cc}^2(t), \\ I_s(t) = \alpha e^{\beta V_{cc}(t)}, \\ E(t) = E(0) - \displaystyle\int_0^t I_s(t) V_{cc}(t)\, \mathrm{d}t, \end{cases} \tag{2}$$

where $E(t)$ is the energy stored in C$_s$ at time t. In (2), the solution of $V_{cc}(t)$ is

$$V_{cc}(t) = -\frac{1}{\beta} \ln\left(e^{-V_0 \beta} + \frac{\alpha\beta}{C_s} t \right), \tag{3}$$

where $V_0 = 3$ V is the initial voltage of C$_s$, i.e., V_{cc} at time 0.

At time t, denote the currents flow through R$_3$ and C$_2$ by $I_0(t)$ and $I_1(t)$, respectively. Let $V(t)$ and $Q(t)$ be the voltage and charge on C$_2$ at time t, respectively. Assume the forward voltage of D$_2$ and base-emitter voltage of T$_2$ are V_f and V_{be}, respectively. According to the capacitor energy formula, we can write the following differential equations to calculate the

I_b with respect to time:

$$\begin{cases} I_b(t)=I_0(t)+I_1(t), \quad I_0(t)R_3=V_f+\dfrac{Q(t)}{C_2} \\ I_1(t)=\dfrac{\mathrm{d}Q(t)}{\mathrm{d}t}, \quad V_{cc}(t)=I_b(t)R_5+\dfrac{Q(t)}{C_2}+V_f+V_{be}, \end{cases} \tag{4}$$

where V_f and V_{be} are both 0.7 V for 1N4148 diode and NSS30071 transistor.

From (4), we can obtain a first-order non-homogeneous differential equation of $Q(t)$:

$$R_5\frac{\mathrm{d}Q(t)}{\mathrm{d}t}+\frac{R_3+R_5}{R_3C_2}Q(t)+V_{cc}(t)+V_f\left(1+\frac{R_5}{R_3}\right)+V_{be}=0, \tag{5}$$

where $Q(0)=0$ and $V_{cc}(t)$ is given in (3). Through derivation, the solution of (5) can be written as follows:

$$Q(t)=\frac{1}{\mathcal{A}(t)}\left\{\gamma\kappa\mathcal{A}(t)-\frac{1}{R_5\beta}\left[\gamma\mathcal{A}(t)\mathcal{B}(t)-\gamma e^{\frac{-\rho}{\gamma\lambda}}(\mathcal{B}(t)+\mathcal{C}(t))\right]\right\}\Bigg|_0^t, \tag{6}$$

where

$$\mathcal{A}(t)=e^{\frac{t}{\gamma}},\ \mathcal{B}(t)=\ln\left(\rho+\lambda t\right),\ \mathcal{C}(t)=\sum_{i=1}^{\infty}\frac{\left[\frac{1}{\gamma\lambda}\left(\rho+\lambda t\right)\right]^i}{i\times i\,!}, \tag{7}$$

and

$$\gamma=\frac{R_3R_5C_2}{R_3+R_5},\ \kappa=-\left(\frac{V_f+V_{be}}{R_5}+\frac{V_f}{R_3}\right),\ \lambda=\frac{\alpha\beta}{C_s},\ \rho=e^{-V_0\beta}. \tag{8}$$

According to (6), it can be obtained that

$$I_b(t)=\frac{V_f}{R_3}+\frac{Q(t)}{R_3C_2}+\frac{Q(t)}{C_2}. \tag{9}$$

Substituting (6) into (9), we can get the analytical expression of I_b with respect to time.

In Fig. 9(a), we show the results calculated with (9). From the figure, it can be observed that the theoretical result matches the experiment very well when $C_2=100\,\mu$F. However, as C_2 decreases, the analytical solution of $I_b(t)$ are gradually away from the measurements. This is reasonable because if C_2 is small, I_b will not be able to stay high for long. Once I_b drops below 0.2 mA, I_s will be much less than that described in the second equation of (2) as the current flow through the collector of T_2 is limited by I_b. Consequently, the supply voltage will decrease much slower with time than that expressed in (3), thereby delaying the drop of based current at T_2.

2) Transmission and Sampling Driver: As introduced in Section III, at 16 MHz clock rate and 3.5 dBm transmission power, the current consumption of the MCU sending packet and sampling data can be as high as 18.4 mA and 28.4 mA, respectively. Therefore, during data transmission and ADC sampling, R_3 should be shorted to provide the MCU sufficient drive current. However, the mechanism designed to temporally short R_3 for MCU startup cannot be applied here as C_2 is fully charged by the startup circuit.

To solve the above problem, an NPN transistor T_1 is connected across the resistor R_3, as shown in Fig. 8. After a successful startup, the MCU can use a general-purpose input/output (GPIO) pin to turn on/off T_1, and then dynamically adjust the drive current. Specifically, before transmission and sampling, the MCU first sets PE3 (one of the GPIO pins) high, which turns on T_1 to short R_3. In this case, a large I_b is generated to drive the MCU for sensing and data sending. After transmission and ADC sampling, PE3 is toggled, thus turning off T_1 to reduce power consumption.

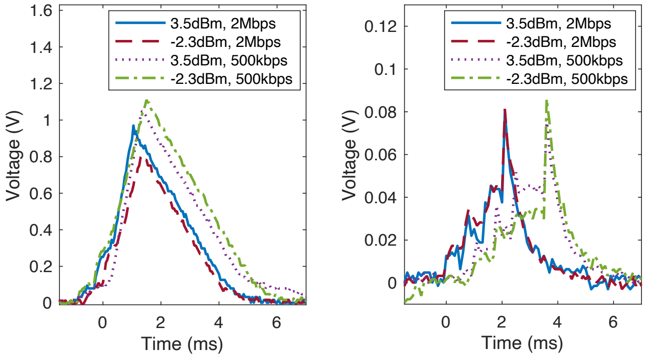

(a) (b)

Figure 10: Performance improvement with transistor T_1 and control signal PE3 for data transmission. (a) V_{ce} of T_2 without T_1. (b) V_{ce} of T_2 with T_1.

In Fig. 10, we show how T_1 affects the performance of the transmission driver. In the figure, the supply voltage, MSDU payload, and MCU clock frequency are 4 V, 105 octets, and 4 MHz, respectively. As illustrated in the figure, without T_1, the base current at T_2 is insufficient to drive the MCU for data transmission. As a result, T_2 enters the unsaturated region, resulting in a large V_{ce}. For example, V_{ce} can reach 1.1 V when the MCU transmits at 3.5 dBm and 500 kbps. In this case, if the V_{cc} is lower than 2.9 V, the MCU that requires 1.8 V supply voltage will not transmit properly. In contrast, if the T_1 is turned on during data transmission, V_{ce} can be reduced by 92.7% to 80 mV. In this situation, the MCU can send data even if V_{ce} is below 1.9 V, which significantly improves the energy utilization.

C. Power Management Circuit

As analyzed in Section III, the energy consumption for MCU startup, transmission and sampling is proportional to the supply voltage. To save energy while reducing the charging time, a power management circuit is needed so that RF-UIoT nodes can operate appropriately with a low supply voltage.

The design of our power management circuit can be found in Fig. 8, which consists of a comparator CP_2, resistors R_6 to R_{10}, a diode D_3, and a capacitor C_3. In the circuit, R_6 and R_7 form a voltage divider circuit. Before each data transmission, the MCU will measure the voltage on R_7 to calculate V_{cc}. If V_{cc} is below a threshold, so called the sleep voltage, the MCU will halt the operation and switches to deep sleep model.

In deep sleep, the power consumption of RF-UIoT is much lower than the energy harvesting rate. According to measurements, the former is less than 100 μW at 2 V supply voltage, while the latter is higher than 1 mW at 2 dBm incident power. Therefore, after a certain time, V_{cc} will be restored. When V_{cc}

reaches a preset threshold, the voltage at the non-inverting input of $\mathrm{CP_2}$ becomes higher than that at the inverting input. The current supply voltage is called the wake-up voltage. At this time, the output of $\mathrm{CP_2}$ generates a rising edge, which can be used as an external interrupt signal INT2 to wake up the MCU. Increasing $\mathrm{R_y}$ can reduce the wake-up voltage, and vice versa. Reducing the resistance of $\mathrm{R_y}$ can increase the wake-up voltage.

Similar to the startup circuit, the dynamic reference voltage created by $\mathrm{R_9}$ and $\mathrm{D_3}$ varies with temperature because the diode's forward voltage decreases linearly with temperature. Hence, we use the NTC thermistor $\mathrm{R_y}$ to compensate for temperature changes in a dynamic environment. According to the experimental results, if the wake-up voltage is set to 3 V, when the ambient temperature is 25°C, $\mathrm{R_y}$ should be $780\,\mathrm{k\Omega}$, and needs to be decreased by $60\,\mathrm{k\Omega}$ for every 5°C increment in temperature.

Here, we define the unit charging time as the time it takes to charge the RF-UIoT for each packet transmission. In Fig. 11, the unit charging time of different power management strategies is evaluated, where the wake-up voltage can be calculated by adding the voltage increment to the sleep voltage. In the experiment, the intensity of radio energy received by the RF-UIoT node is 2 dBm. The MCU clock frequency, wireless transmission power, data rate, and MSDU payload are 8 MHz, 3.5 dBm, 1 Mbps, and 105 octets, respectively. Before sending each data packet, the ADC samples 10 times for environmental monitoring.

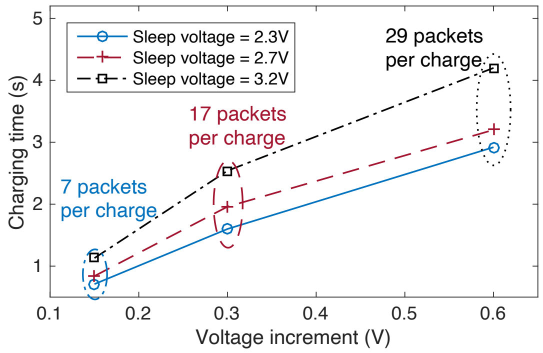

Figure 11: Performance with power management strategies.

As shown in Fig. 11, for strategies that continuously send the same amount of packets, the one using a low wake-up voltage can significantly reduce the unit charging time. Specifically, as introduced in Section. III-B, the energy consumption of the MCU for data transmission is proportional to the supply voltage. Therefore, sending data at low supply voltage can improve the energy efficiency. For example, if set the sleep voltage and wake-up voltage to 2.3 V and 2.45 V, respectively, it takes the RF transmitter only 0.71 s to charge the RF-UIoT node, and then the node can successfully transmit 7 data packets before sleeping. With this strategy, the unit charging time is 101 ms. In contrast, if the sleep voltage and wake-up voltage are increased by 0.9 V, the transmitter needs to charge the node 1.13 s to send 7 packets. In this case, the unit charging time is increased to 161 ms, 1.6 times over the previous strategy.

In addition, from Fig. 11 it can be observed that if the sleep voltage is the same, the strategy with higher wake-up voltage can continuously send more packets to reduce the unit charging time because it reduces the frequency of waking up nodes. Using the strategies with 3.2 V sleep voltage as an example, if the wake-up voltage is set to 3.8 V, the transmitter needs 4.2 s to charge the node. However, with this strategy, the node only needs to be awaken once and then can continuously send 29 packets before sleeping. In this case, the unit charging time is 145 ms. However, if the wake-up voltage is set to 3.35 V, although it takes only 1.13 s to change the node, the number of packets that the node can sent is also reduced to 7. In this case, the node needs to be awaken 5 times to send 29 packets. As a result, the unit charging time increases to 161 ms, 10% higher than the previous strategy.

According to the above analysis, in order to reduce the unit charging time, the power management circuit should use low sleep voltage and high wake-up voltage, so that the RF-UIoT node can continuously transmit as much data as possible every time it wakes up.

D. RF-UIoT System Integration Test

We conducted RF-UIoT system integration test in the lab environment. The experiment setup is shown in Fig. 12 (a). In the figure, the Agilent 8648A signal generator produces 915 MHz CW at 2 dBm to charge the P1110B energy harvester. The Agilent MSO6032 oscilloscope is used to monitor the supply voltage and the INT2 interrupt generated by the comparator $\mathrm{CP_2}$ in the control circuit. The Keysight CX3324 current analyzer tracks the current waveform of the MCU, while multimeters measure the output of the comparator $\mathrm{CP_1}$ and the voltage drop between the collector and emitter of the transistor $\mathrm{T_2}$.

V_{cc} and V_{out} in Fig. 12 (b) are indications to the supply voltage of P1110B harvester and output voltage provided to the MCU, respectively. With 2 dBm input power, V_{cc} is charged to 1.8 V in 3 seconds. Note that the MCU will automatically startup if without the Startup circuit but will never be successfully activated due to the significant voltage drop during startup. With our Startup circuit, V_{cc} is charged to 3.2 V at t_1 (i.e., in about 10 seconds). The startup process takes about 100 ms. After successfully power-up at t_2, it transmits 1 kilobyte of data between t_2 and t_3 (i.e., transmission power is 3.5 dBm, payload is 105 octets). Due to the dropping voltage, MCU enters the deep sleep model at time t_3 (i.e., V_{cc} = 2.3 V) to save energy. With 1.6 seconds of further charging, the MCU reactivates at t_4 when V_{cc} reaches wake-up voltage and transmits 1.7 kilobyte of data before sleeping at t_5. The startup voltage and the wake-up voltage can be adjusted by changing R_x and R_y shown in Fig. 8, respectively. We can adjust the sleeping threshold by programing MCU.

E. Discussions

In practical applications, the RF-UIoT node will enter deep sleep mode when the UAV moves out of range in order to conserve energy for soil sensing in the absence of an external power source. The RF-UIoT can wake up to measure

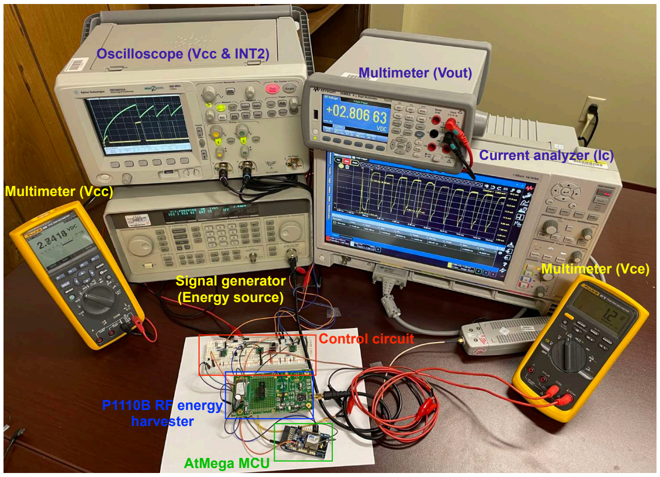

(a) RF-UIoT system integration test

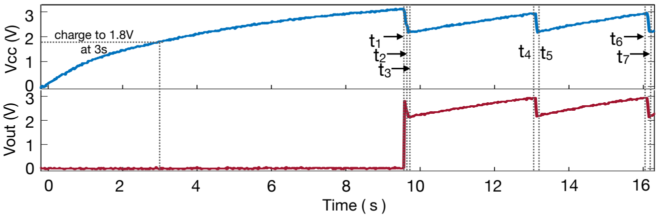

(b) Voltage waveform of Vcc and Vout

Figure 12: RF-UIoT system integration test and voltage waveform.

soil parameters until the harvested energy is depleted. In the subsequent charging cycle, the latest sensing results, along with the recorded historical data, will be transmitted to UAV.

The operational duration of an RF-UIoT node within a single charging cycle is influenced by several factors, such as the capacity of the supercapacitor, the power consumption of the RF-UIoT in deep sleep mode, and the sensing frequency. For instance, the ATmega256RFR2 wireless board demonstrates very low power consumption (as low as 0.5 μA) in deep sleep mode. According to our present design, the RF-UIoT is anticipated to function for several hours after being charged to 3.3 V. Enhancing the supercapacitor's capacity or utilizing a Microchip eXtreme low-power (XLP) MCU with sleep currents as low as 9 nA [23] could further prolong the RF-UIoT's operation to multiple days after the UAV departs the area. In such scenarios, a weekly UAV flight frequency of once or twice can sustain daily soil sensing activities. To attain a higher temporal resolution, the UAV flight frequency can be effortlessly increased to a daily basis. RF-UIoT offers user-customizable temporal resolution, which presents a substantial advantage compared to the fixed temporal resolution of satellite remote sensing.

Utilizing drones to gather soil sensing data from RF-UIoTs is considerably more cost-effective than traditional laboratory soil measurements and provides greater flexibility and efficacy compared to remote sensing. Consequently, UAV remotely-powered RF-UIoT emerges as a promising solution for delivering long-term, scalable, and automated *in situ* soil monitoring.

V. RELATED WORK

RF energy harvesting circuit design: In the area of energy harvesting system design, previous research has primarily focused on how to efficiently harvest RF energy (i.e., energy harvester circuit design) [7], [24]–[26]. By optimizing circuit design, RF harvesters can achieve energy conversion efficiencies of up to 70%, with input sensitivity as high as -35 dBm [25]. While these harvesters employ different design strategies, they share a common issue when directly connected to IoT boards. Specifically, the IoT board will enter its startup procedure once the capacitor voltage reaches a threshold. However, due to the low average energy harvesting rate relative to the power consumption required for startup, the IoT board will continually consume energy received from the harvester without ever successfully activating. This challenge motivated us to develop a startup circuit for RF energy harvesting-powered IoT devices.

RF energy harvesting powered wireless communications: One focus of this research area is on optimal transmission strategy design aiming to maximize the efficiently utilize the harvested energy [27], [28]. The optimal transmission power is adjusted based on the fluctuation of incident RF energy through solving a nonlinear optimization problem. The performance evaluation of transmission strategies rely on theoretical analysis and simulations since real implementation is not feasible due to a lot of practical limitations. Different from these existing software-based transmission control, we develop hardware-based power management circuits that can operates when MCU is *OFF*.

Powering underground sensors: The combination of rechargeable battery and solar panel is the most popular power solution and is widely used in the commercial soil sensing products [5]. However, its aboveground components would cause interference to tillage and planting operations and significantly limit the spatial resolution of deployment. The battery-only nodes buried in soil can provide non-disruptive sensing. However, due to limited battery capacity, temporal resolution or longevity must be sacrificed to avoid frequent battery replacement. Magnetic induction (MI) is another promising method to powering UIoTs [29]–[31]. However, MI-based wireless charging requires large coil antennas and precise coil alignment [31], making it less attractive for large-scale deployments and mobile applications. [11]–[13] proposed to use RF energy to charge underground nodes. However, the dropping supply voltage, the high energy attenuation in soil and the dynamic energy consumption introduce a lot of challenges making it feasible in practice. This motivates us to develop startup, drive and power management circuits for RF-UIoTs.

Underground wireless communications: Underground wireless communications have been widely used in underground mines, pipeline monitoring, and agriculture applications. Existing research has been focusing on underground signal propagation modeling [16], [17], with the main design goals being to improve the communication range and maximize the transmission rate. Underground communication is not the focus of this paper. We used a commercial Microchip ATmega256RFR2 ZigBee board for communications. However, the proposed RF-UIoT prototype can be easily extended to other communication techniques (e.g., LoRa, BLE, etc.).

VI. CONCLUSION

In this article, we developed an RF-UIoT for long-term, scalable and automated *in-situ* soil monitoring. The RF-UIoT nodes, buried in soils, can harvest 915 MHz radio energy radiated from UAV for sensing and wireless communications. Our experimental results demonstrated that with an RF transmitter of 36 dBm EIPR and 40% soil moisture, RF-UIoT nodes buried 15 cm deep can receive an average of 2 dBm in radio energy. To enhance energy efficiency and ensure reliable operation, we designed a control circuit to drive the node and manage the harvested energy. This control circuit significantly extends the harvesting range of RF-UIoT with mobile energy sources or allows it to be buried deeper than current solutions. We built a prototype RF-UIoT node using off-the-shelf components. Our tests show that after 10 seconds of wireless charging with 2 dBm input power, the node successfully starts up, transmitting more than 1 kilobyte of data at 3.5 dBm transmission power, followed by an additional 1.7 kilobytes of data with every 1.6 seconds further charging. The RF-UIoT system has the potential to revolutionize the way soil monitoring and industrial agriculture are conducted by eliminating the need for batteries or aboveground attachments, thereby increasing efficiency and reducing costs.

ACKNOWLEDGEMENT

This work is supported in part by the US National Science Foundation under Awards CIF-2051356, CNS-2122167, and CNS-2122159.

REFERENCES

[1] Y. Wang, X. Duan, and L. Wang, "Spatial distribution and source analysis of heavy metals in soils influenced by industrial enterprise distribution: case study in Jiangsu Province," *Science of the Total Environment*, vol. 710, p. 134953, 2020.

[2] I. Charania and X. Li, "Smart farming: Agriculture's shift from a labor intensive to technology native industry," *Internet of Things*, vol. 9, p. 100142, 2020.

[3] E. Babaeian, M. Sadeghi, S. B. Jones, C. Montzka, H. Vereecken, and M. Tuller, "Ground, proximal, and satellite remote sensing of soil moisture," *Reviews of Geophysics*, vol. 57, no. 2, pp. 530–616, 2019.

[4] T. W. Ford and S. M. Quiring, "Comparison of contemporary in situ, model, and satellite remote sensing soil moisture with a focus on drought monitoring," *Water Resources Research*, vol. 55, no. 2, pp. 1565–1582, 2019.

[5] P. Sanjeevi, S. Prasanna, B. Siva Kumar, G. Gunasekaran, I. Alagiri, and R. Vijay Anand, "Precision agriculture and farming using internet of things based on wireless sensor network," *Transactions on Emerging Telecommunications Technologies*, vol. 31, no. 12, p. e3978, 2020.

[6] Y. Liu, X. Ma, L. Shu, G. P. Hancke, and A. M. Abu-Mahfouz, "From Industry 4.0 to Agriculture 4.0: Current status, enabling technologies, and research challenges," *IEEE Transactions on Industrial Informatics*, vol. 17, no. 6, pp. 4322–4334, 2020.

[7] X. Lu, P. Wang, D. Niyato, D. I. Kim, and Z. Han, "Wireless networks with RF energy harvesting: a contemporary survey," *IEEE Communications Surveys & Tutorials*, vol. 17, no. 2, pp. 757–789, 2014.

[8] Y. Luo and L. Pu, "Practical issues of RF energy harvest and data transmission in renewable radio energy powered IoT," *IEEE Transactions on Sustainable Computing*, vol. 6, no. 4, pp. 667–678, 2020.

[9] R. Du, T. O. Timoudas, and C. Fischione, "Comparing backscatter communication and energy harvesting in massive IoT networks," *IEEE Transactions on Wireless Communications*, vol. 21, no. 1, pp. 429–443, 2021.

[10] S. D. Assimonis, S.-N. Daskalakis, and A. Bletsas, "Sensitive and efficient RF harvesting supply for batteryless backscatter sensor networks," *IEEE Transactions on Microwave Theory and Techniques*, vol. 64, no. 4, pp. 1327–1338, 2016.

[11] G. Liu, Z. Wang, and T. Jiang, "Qos-aware throughput maximization in wireless powered underground sensor networks," *IEEE Transactions on Communications*, vol. 64, no. 11, pp. 4776–4789, 2016.

[12] U. Raza and A. Salam, "On-site and external energy harvesting in underground wireless," *Electronics*, vol. 9, no. 4, p. 681, 2020.

[13] Y. Liu, D. Li, B. Du, L. Shu, and G. Han, "Rethinking Sustainable Sensing in Agricultural Internet of Things: From Power Supply Perspective," *IEEE Wireless Communications*, 2022.

[14] K. Lin and T. Hao, "Experimental link quality analysis for LoRa-based wireless underground sensor networks," *IEEE Internet of Things Journal*, vol. 8, no. 8, pp. 6565–6577, 2020.

[15] B. Silva, R. M. Fisher, A. Kumar, and G. P. Hancke, "Experimental link quality characterization of wireless sensor networks for underground monitoring," *IEEE Transactions on Industrial Informatics*, vol. 11, no. 5, pp. 1099–1110, 2015.

[16] A. Salam and M. C. Vuran, "Impacts of soil type and moisture on the capacity of multi-carrier modulation in internet of underground things," in *International conference on computer communication and networks (ICCCN)*. IEEE, 2016, pp. 1–9.

[17] A. R. Silva and M. C. Vuran, "Communication with aboveground devices in wireless underground sensor networks: An empirical study," in *2010 IEEE international conference on communications*. IEEE, 2010, pp. 1–6.

[18] Powercast Corporation, *P2110B — 915 MHz RF power harvester receiver*, Powercast Corporation, Pittsburgh, PA, U.S.A., December 2016.

[19] ——, *P1110B — 915 MHz RF power harvester receiver*, Powercast Corporation, Pittsburgh, PA, U.S.A., August 2018.

[20] Y. Luo and L. Pu, "WUR-TS: Semi-passive wake-up radio receiver based time synchronization method for energy harvesting wireless networks," *IEEE Transactions on Mobile Computing*, 2021.

[21] Microchip Technology, *Atmel ATmega256RFR2 datasheet*, Microchip Technology, Chandler, AZ, U.S.A., September 2014.

[22] Onsemi Company, *NSS30071MR6T1G Transistor*, Onsemi Company, Phoenix, AZ, USA, June 2005.

[23] Microchip Technology, "8-bit Low-Power PIC and AVR Microcontrollers," microchip.com, 2023, [Accessed: Jan, 2023]. [Online]. Available: https://www.microchip.com/en-us/solutions/low-power/8-bit-low-power-mcus

[24] D. Masotti, A. Costanzo, P. Francia, M. Filippi, and A. Romani, "A load-modulated rectifier for rf micropower harvesting with start-up strategies," *IEEE Transactions on Microwave Theory and Techniques*, vol. 62, no. 4, pp. 994–1004, 2014.

[25] C. Song, Y. Huang, J. Zhou, J. Zhang, S. Yuan, and P. Carter, "A high-efficiency broadband rectenna for ambient wireless energy harvesting," *IEEE Transactions on Antennas and Propagation*, vol. 63, no. 8, pp. 3486–3495, 2015.

[26] I. Chaour, A. Fakhfakh, and O. Kanoun, "Enhanced passive RF-DC converter circuit efficiency for low RF energy harvesting," *Sensors*, vol. 17, no. 3, p. 546, 2017.

[27] Y. Luo, L. Pu, and L. Lei, "Impact of varying radio power density on wireless communications of RF energy harvesting systems," *IEEE Transactions on Communications*, 2020.

[28] A. Biason and M. Zorzi, "On the effects of battery imperfections in an energy harvesting device," in *Proceedings of International Conference on Computing, Networking and Communications*. IEEE, 2016, pp. 1–7.

[29] N. Saeed, M.-S. Alouini, and T. Y. Al-Naffouri, "Toward the internet of underground things: a systematic survey," *IEEE Communications Surveys & Tutorials*, vol. 21, no. 4, pp. 3443–3466, 2019.

[30] S. Kisseleff, I. F. Akyildiz, and W. H. Gerstacker, "Survey on advances in magnetic induction-based wireless underground sensor networks," *IEEE Internet of Things Journal*, vol. 5, no. 6, pp. 4843–4856, 2018.

[31] S. Kisseleff, X. Chen, I. F. Akyildiz, and W. H. Gerstacker, "Efficient charging of access limited wireless underground sensor networks," *IEEE Transactions on Communications*, vol. 64, no. 5, pp. 2130–2142, 2016.